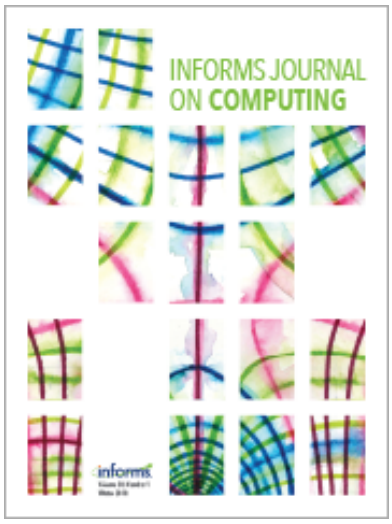

INFORMS Journal on Computing

Publication details, including instructions for authors and subscription information:
http://pubsonline.informs.org

Spatiotemporally Optimal Fractionation in Radiotherapy

Fatemeh Saberian, Archis Ghate, Minsun Kim

To cite this article:
Fatemeh Saberian, Archis Ghate, Minsun Kim (2017) Spatiotemporally Optimal Fractionation in Radiotherapy. INFORMS Journal on Computing 29(3):422-437. https://doi.org/10.1287/ijoc.2016.0740

http://pubsonline.informs.org/journal/ijoc/

INFORMS JOURNAL ON COMPUTING
Vol. 29, No. 3, Summer 2017, pp. 422–437
ISSN 1091-9856 (print), ISSN 1526-5528 (online)

Spatiotemporally Optimal Fractionation in Radiotherapy

Fatemeh Saberian,[a] **Archis Ghate,**[a] **Minsun Kim**[b]

[a] Department of Industrial and Systems Engineering, University of Washington, Seattle, Washington 98195; [b] Department of Radiation Oncology, University of Washington, Seattle, Washington 98195

Contact: saberian@uw.edu (FS); archis@uw.edu (AG); mk688@uw.edu (MK)

Received: April 15, 2015
Revised: December 26, 2015; May 22, 2016; August 12, 2016; September 27, 2016
Accepted: October 6, 2016
Published Online: May 24, 2017

https://doi.org/10.1287/ijoc.2016.0740

Abstract. We present a spatiotemporally integrated formulation of the optimal fractionation problem using the standard log-linear-quadratic survival model. Our objective is to choose a fluence map and a number of fractions to maximize the biological effect of tumor dose averaged over its voxels subject to maximum dose, mean dose, and dose-volume constraints for various normal tissues. Constraints are expressed in biologically effective dose equivalents. We propose an efficient convex programming method to approximately solve the resulting computationally difficult model.

Through extensive computer simulations on 10 head-and-neck and prostate cancer test cases with a broad range of radiobiological parameters, we compare the biological effect on tumors obtained by our integrated approach relative to that from two other models. The first is a traditional intensity modulated radiation therapy (IMRT) fluence map optimization model that does not optimize the number of fractions. The second assumes that a fluence map is available a priori from a traditional IMRT optimization model and then optimizes the number of fractions, thus separating the spatial and temporal components.

The improvements in tumor biological effect over IMRT were 9%–52%, with an average of 22% for head-and-neck, and 53%–108%, with an average of 69% for prostate. The improvements in tumor biological effect over the spatiotemporally separated model were 15%–45%, with an average of 27%, and 17%–23%, with an average of 21%, for head-and-neck and prostate, respectively. This suggests that integrated optimization of the fluence map and the number of fractions could improve treatment efficacy, as measured within the linear-quadratic framework.

History: Accepted by Allen Holder, Area Editor for Applications in Biology, Medicine, and Health Care.
Funding: This research was funded in part by the National Science Foundation [Grant CMMI 1054026].

Keywords: intensity modulated radiation therapy • convex programming • linear quadratic model

1. Introduction

In external beam radiotherapy, radiation damages both the cancer cells and the normal tissue. Thus, the goal is to maximize damage to the tumor while limiting toxic effects on nearby normal tissue. This is attempted by spatial localization and temporal dispersion of radiation dose.

Spatial localization is achieved by prescribing a high dose to the cancerous region and putting upper limits on the dose to healthy anatomies. The well-developed intensity modulated radiation therapy (IMRT) technology, and the associated spatial optimization models and solution algorithms are employed to optimize the radiation intensity profile (also called the fluence map). One standard formulation of this problem minimizes the total squared deviation of the doses delivered to all voxels in the tumor from the tumor prescription dose. This spatial side of radiation therapy has been studied extensively (Burman et al. 1997, Ehrgott et al. 2008, Eisbruch 2002, Langer et al. 2003, Romeijn et al. 2006, Shepard et al. 1999, Webb 2010).

On the temporal side, the prevalent strategy is to break the total planned dose into multiple, well-separated treatment sessions, called fractions, that are administered over several weeks. An identical dose is planned for each fraction; this is called equal-dosage fractionation. Since normal cells typically have better damage-repair capabilities than tumor cells, such temporal dispersion gives the normal tissue some time to recover between sessions. For many tumors, using a large number of fractions with a small dose in each fraction may allow the treatment planner to administer a larger total tumor dose than using a small number of fractions with a large dose in each fraction. Thus, it would seem that for these tumors, the longer the treatment course, the better. However, tumors may proliferate over the treatment course, in which case shorter treatment courses are believed to work better as they kill tumor cells quickly before significant proliferation. Moreover, there is an increasing interest in shorter treatment courses, because they are logistically more convenient. Such tradeoffs in determining an optimal

number of fractions have been clinically studied over the last several decades (Ahamad et al. 2005; Arcangeli et al. 2010; Fu et al. 2000; Garden 2001; Ho et al. 2009; Horiot et al. 1997, 1992; Kader et al. 2011; Marzi et al. 2009; Rockwell 1998; Trotti et al. 2005). This question of choosing the number of fractions and the corresponding dose per fraction is generally referred to as the *optimal fractionation problem*.

The standard thought process in the optimal fractionation problem is to maximize the biological effect (BE) of a radiation dose on the tumor subject to an upper bound constraint on the biologically effective dose (BED) delivered to the normal tissue (Hall and Giaccia 2005). The linear-quadratic (LQ) model is commonly employed for quantifying tumor BE and normal tissue BED (Hall and Giaccia 2005). Existing research on optimal fractionation based on the LQ framework is limited to stylized formulations that often lead to a closed-form formula for the optimal number of fractions. This formula is derived using single-variable calculus. The literature on this includes Armpilia et al. (2004), Bortfeld et al. (2015), Fowler (1990, 2001, 2007, 2008), Fowler and Ritter (1995), Jones et al. (1995), Keller et al. (2012), Mizuta et al. (2012), Unkelbach et al. (2013b). Table 1 summarizes the contributions of these models.

One limitation of most existing stylized models is that they only consider a single normal tissue. This not only may lead to an incorrect prediction of the number of fractions, but it also may yield a dose that cannot be tolerated by other nearby normal tissues that were excluded from the formulation. This important concern stems from the fact that essentially all anatomical regions of interest include multiple normal tissues. Moreover, the optimal number of fractions in reality depends not only on the relative difference between the tumor's and the normal tissue's response to radiation but also on the anatomy of the cancerous region with respect to the positioning of the radiation fields. Thus, another limitation of the above stylized models is that they do not explicitly model intensity modulation and essentially ignore the spatial side of the problem even though IMRT technology is now ubiquitous. Such limitations curtail the practical applicability of these stylized models; they were addressed in our recent work in Saberian et al. (2016).

Although our model in Saberian et al. (2016) is currently the most comprehensive formulation of the optimal fractionation problem based on the LQ framework, it has an important limitation—it separated the spatial and temporal components of the problem. That is, a spatially optimized fluence map was assumed to be available a priori and the number of fractions was then optimized with respect to this map using the concept of sparing factors. This approach simplified the optimal fractionation problem considerably—we were able to characterize the BE on a tumor as a quasiconcave function of the number of fractions, which led to a simple procedure for optimizing this number. Unfortunately, this approach is suboptimal, especially because the spatial optimization problem that is solved a priori does not directly depend on any biological dose-response parameters of the tumor or the normal tissue.

In this paper, we address the above limitations by proposing a spatiotemporally integrated optimal fractionation model where the fluence map and the number of fractions are both optimization variables. This formulation is computationally difficult to solve. We thus propose an efficient algorithm rooted in convex programming for its approximate solution. Our computer simulations on head-and-neck and prostate cancer test cases suggest that, within the LQ framework, even approximate solution of our computationally difficult, spatiotemporally integrated model may offer some benefit over solving existing stylized models.

2. Problem Formulation

Consistent with existing stylized models of the optimal fractionation problem, our overall methodology is to choose a fluence map and a number of fractions to maximize the BE of average dose over all tumor voxels subject to BED constraints on normal tissues. The mathematical notation and terminology here are standard in the literature and are borrowed from our recent work in Saberian et al. (2016).

2.1. Expression for the Tumor Objective Function

Let n denote the number of tumor voxels, indexed by $i = 1, 2, \ldots, n$. The radiation field is discretized into small segments called *beamlets*. Let k be the number of beamlets and let $u \in \mathfrak{R}^k_+$ denote the

Table 1. A Summary of Some Optimal Fractionation Models That Use the LQ Framework

References	≥ 2 normal tissues	Closed form for dose	Spatiotemporally optimal
Fowler (1990, 2001, 2007, 2008), Fowler and Ritter (1995)	No	No	No
Armpilia et al. (2004), Jones et al. (1995)	No	Yes	No
Yang and Xing (2005)	Yes	No	No
Mizuta et al. (2012)	No	Yes	No
Bortfeld et al. (2015), Keller et al. (2012), Unkelbach et al. (2013b)	No	Yes	No
Saberian et al. (2016)	Yes	Yes	No

k-dimensional beamlet intensity vector used in each treatment session. Let A be the $n \times k$ nonnegative tumor dose deposition matrix and let A_i denote its ith row, which corresponds to the ith tumor voxel. That is, according to the standard linear dose deposition model (Jeraj and Keall 1999, Siebers et al. 2001, Spirou and Chui 1998, Tian et al. 2013, Webb and Oldham 1996), $A_i u$ is the dose delivered to the ith tumor voxel and $\bar{A}u \triangleq (\sum_{i=1}^{n} A_i u)/n$ is the average dose over all tumor voxels in each session.

Now consider a treatment course with N once-daily fractions. Let T_{double} (days) denote the doubling time for the tumor and T_{lag} (days) denote the time lag after which tumor proliferation starts after treatment initiation. The expression $[(N-1)-T_{\text{lag}}]^+$, which is defined as $\max((N-1)-T_{\text{lag}}, 0)$, is the time over which the tumor proliferates. We define

$$\tau(N) \triangleq \frac{[(N-1)-T_{\text{lag}}]^+ \ln 2}{T_{\text{double}}} \tag{1}$$

and let α_0 and β_0 denote the parameters of the LQ model for the tumor. Then, according to the LQ model, the total N-session BE of the average tumor dose is given by

$$N\alpha_0(\bar{A}u) + N\beta_0(\bar{A}u)^2 - \tau(N). \tag{2}$$

We wish to choose N within a clinically viable range $1 \le N \le N_{\max}$ and a fluence map u to maximize (2). This objective is nonconvex in u because we are maximizing a convex function. Fortunately, we are able to show in Section 3 that this objective can be easily rewritten in a convex (in fact, linear) form. This is achieved by observing that, when N is fixed, maximizing (2) is equivalent to maximizing $\bar{A}u$, a linear function.

Note here that, as is common in IMRT, there are other possible choices for the objective function in this formulation. One option is to maximize the BE of the minimum tumor dose over all voxels. It turns out that, similar to our objective function, this alternative objective function can also be converted into a convex (in fact, linear) form. This is achieved by observing that, when N is fixed, maximizing the BE of the minimum tumor dose is equivalent to maximizing the minimum tumor dose itself; the minimum tumor dose can be maximized by instead maximizing a new variable t and adding a linear constraint for each tumor voxel, enforcing that the dose to this voxel is at least t (also see Section 4.4).

Both the average tumor dose and the minimum tumor dose are special cases of the well-known concept of generalized equivalent uniform dose (gEUD) (Choi and Deasy 2002). This gEUD is parameterized by a single parameter p, and is given by

$$\text{gEUD} \triangleq \left(\sum_{i=1}^{n} (A_i u)^p / n \right)^{1/p}. \tag{3}$$

The gEUD can be seen as a generalized average; it is well known that it reduces to the average tumor dose when $p = 1$ and to the minimum tumor dose as $p \to -\infty$ (see Choi and Deasy 2002). Thus, both our approach of maximizing the BE of the average tumor dose and the aforementioned alternative approach of maximizing the BE of the minimum tumor dose can be seen as maximizing the BE of a particular tumor gEUD. Consequently, both these choices of objective functions are consistent with the original motivation for the concept of EUD (see Niemierko 1997). We decided not to use the alternative maximin objective function because, as one would expect in a formulation that maximizes the worst case BE, it led to fluence-maps that were too conservative in our preliminary numerical experiments.

Another possibility for the objective function is to maximize the average BE of the doses delivered to all tumor voxels. This alternative, nonconvex objective is perhaps biologically more meaningful because it adds the BE over individual voxels to quantify the combined effect. Interestingly, the standard approach for solving this nonconvex problem reduces to using our objective in expression (2). The reasoning for this is as follows. The alternative nonconvex objective function cannot be equivalently written in a convex form. The resulting optimization problem is thus computationally intractable. The standard approach for approximate solution of such problems is to instead solve a relaxation of the objective function (see, for example, the literature review in Luo et al. 2010). The standard relaxation of the alternative objective is based on the fact that the sum of squares is no bigger than the square of the sum; this relaxation of the alternative objective function yields our objective function in (2).

We next describe our constraints in detail.

2.2. Normal Tissue Tolerance and Fluence Map Smoothness Constraints

Let $O_1, O_2, \ldots, O_M$ denote the M different normal tissues under consideration. Let $\mathcal{M} = \{1, \ldots, M\}$ be the set of indices of these normal tissues. For $m \in \mathcal{M}$, let n_m denote the number of voxels in O_m. These voxels are indexed by $j = 1, 2, \ldots, n_m$. Let $\mathcal{N}_m$ denote the set $\{1, 2, \ldots, n_m\}$ of these voxels. All normal tissue voxels are assumed to have equal volume. Let A^m be the $n_m \times k$, nonnegative dose deposition matrix for O_m. Let A_j^m be the jth row of this matrix; this is the row that corresponds to the jth voxel in O_m (that is, $A_j^m u$ is the dose delivered to the jth voxel in O_m in each session). Let α_m and β_m be the parameters of the LQ model for normal tissue O_m, and we define $\rho_m \triangleq 1/(\alpha_m/\beta_m)$ for brevity. Then the BED of the dose delivered to the jth voxel in O_m over N fractions is given by

$$N(A_j^m u) + \rho_m N(A_j^m u)^2. \tag{4}$$

Our model includes the three most common types of constraints on normal tissues: maximum dose constraints, mean dose constraints, and dose-volume constraints.

2.2.1. Maximum BED Constraints for Serial Normal Tissues. Let $\mathcal{M}_1 \subseteq \mathcal{M}$ be the set of indices of serial normal tissues for which we wish to include maximum dose constraints. These are the normal tissues whose function is hampered even when a small region is damaged by radiation. Suppose, for any $m \in \mathcal{M}_1$, that a total dose $D^m_{\max}$ is known to be tolerated by each voxel in O_m if administered in N^m_{conv} equal-dose fractions. The BED of this schedule equals

$$\text{BED}^m_{\max} = D^m_{\max}(1 + \rho_m(D^m_{\max}/N^m_{\text{conv}})). \tag{5}$$

We use the standard approach of comparing normal tissue BED. Thus, a dose of $N(A^m_j u)$ over N fractions can be tolerated by the jth voxel in normal tissue O_m if

$$N(A^m_j u) + N\rho_m(A^m_j u)^2 \le \text{BED}^m_{\max}, \quad \forall\, j \in \mathcal{N}_m. \tag{6}$$

Thus, for each $m \in \mathcal{M}_1$, our problem formulation will include constraints (6).

2.2.2. Mean BED Constraints for Parallel Normal Tissues. Let $\mathcal{M}_2 \subseteq \mathcal{M}$ be the set of indices of parallel normal tissues for which we wish to include mean dose constraints. These are normal tissues, where a sufficiently small portion can be damaged without affecting the organ function. Suppose, for any $m \in \mathcal{M}_2$, that mean dose D^m_{mean} is known to be tolerated by O_m if administered in N^m_{conv} equal-dose fractions. The BED of this mean dose is given by

$$\text{BED}^m_{\text{mean}} = D^m_{\text{mean}}(1 + \rho_m(D^m_{\text{mean}}/N^m_{\text{conv}})). \tag{7}$$

Then for normal tissue O_m, we write the mean BED constraint as

$$\frac{N\sum_{j=1}^{n_m}(A^m_j u) + N\rho_m \sum_{j=1}^{n_m}(A^m_j u)^2}{n_m} \le \text{BED}^m_{\text{mean}}. \tag{8}$$

There is a subtle difference between the left-hand side of this inequality and the right-hand side. The left-hand side quantifies the average BED of doses delivered to different voxels; the right-hand side quantifies the BED of the average dose delivered to different voxels. An alternative way to express the left-hand side is to use the BED of average dose, tat is, to write

$$N(\bar{A}^m u) + N\rho_m(\bar{A}^m u)^2 \le \text{BED}^m_{\text{mean}}, \tag{9}$$

where $\bar{A}^m u \triangleq \sum_{j=1}^{n_m} A^m_j u/n_m$ is the average dose. However, the left-hand side of our quadratic constraint (8) is biologically more meaningful than the alternative expression in (9) because it adds the BED for individual voxels to construct the combined effect. The left-hand side in (8) also leads to a more conservative fluence map because it is an upper bound in (9) owing to the aforementioned property about sum of squares. In contrast, there are two benefits to using the alternative expression in (9). First, it makes the left-hand side consistent with the right-hand side. Second, this alternative constraint can be equivalently expressed in terms of a linear constraint on the average dose (in Section 3, we show how to do this in the context of inequality (6), and the conversion would be identical for inequality (9)). This latter constraint will be a computational advantage, as a single linear constraint will be easier to handle than the convex quadratic constraint in (8). Nevertheless, we decided to use the constraint in (8) for its aforementioned clinically sound foundation despite it being computationally more challenging than the linearized equivalent of constraint (9).

2.2.3. Dose-Volume Constraints for Parallel Normal Tissues. Let $\mathcal{M}_3 \subseteq \mathcal{M}$ be the set of indices of normal tissues with dose-volume constraints. Suppose for any $m \in \mathcal{M}_3$ that no more than a volume fraction ϕ_m of normal tissue O_m can receive a dose more than D^m_{dv} if administered in N^m_{conv} fractions. The BED of total dose D^m_{dv} administered in N^m_{conv} equal-dosage fractions is given by

$$\text{BED}^m_{\text{dv}} = D^m_{\text{dv}}(1 + \rho_m(D^m_{\text{dv}}/N^m_{\text{conv}})). \tag{10}$$

Since all voxels in O_m have equal volume, the volume fraction is the same as the voxel fraction. For each $m \in \mathcal{M}_3$ and for $j = 1, 2, \ldots, n_m$, we thus define binary-valued functions $f^m_j(N, u)$ as

$$f^m_j(N,u) = \begin{cases} 1 & \text{if } N(A^m_j u) + N\rho_m(A^m_j u)^2 > \text{BED}^m_{\text{dv}}, \\ 0 & \text{if } N(A^m_j u) + N\rho_m(A^m_j u)^2 \le \text{BED}^m_{\text{dv}}. \end{cases} \tag{11}$$

In words, $f^m_j(N, u)$ is 1 if the BED of dose delivered by fluence map u to voxel j in N sessions exceeds the tolerance BED^m_{dv}; $f^m_j(N, u)$ is 0 otherwise. We use the integer K_m to denote $\lfloor n_m\phi_m \rfloor$, that is, the largest integer that is at most $n_m\phi_m$. Then the dose-volume constraints are written in our optimization model as

$$\sum_{j=1}^{n_m} f^m_j(N,u) \le K_m, \quad m \in \mathcal{M}_3. \tag{12}$$

These constraints ensure that there are at most K_m voxels for which $N(A^m_j u) + N\rho_m(A^m_j u)^2 > \text{BED}^m_{\text{dv}}$; in other words, there are at least $n_m - K_m$ voxels for which $N(A^m_j u) + N\rho_m(A^m_j u)^2 \le \text{BED}^m_{\text{dv}}$. For simplicity, we have assumed that there is at most one dose-volume constraint for each normal tissue. This assumption is not needed anywhere in our algorithm and hence can be removed. In fact, we do this in our computational experiments for prostate cancer in Section 4.

2.2.4. Fluence Map Smoothness Constraints. To ensure that the intensity profile is deliverable in practice using a multileaf collimator, we put a smoothness constraint on each radiation field (Breedveld et al. 2006, Webb et al. 1998). In particular, for each radiation field, we bound the absolute relative difference between intensities of each pair of nearest neighbor beamlets by a fraction ϵ. Then the smoothness constraints can be written compactly in matrix format as $Su \le 0$, where S is a block diagonal matrix with entries $-(1+\epsilon)$, $(1-\epsilon)$, -1, 0, $+1$ at appropriate locations. We are now ready to provide our complete optimization model.

2.3. Complete Optimization Model

Based on the previous discussion, we formulate the optimal fractionation problem as

$$[\mathrm{P}] \quad F^* = \max_{N,u} \{N\alpha_0(\bar{A}u) + N\beta_0(\bar{A}u)^2 - \tau(N)\}, \tag{13}$$

$$N(A_j^m u) + N\rho_m (A_j^m u)^2 \le \mathrm{BED}_{\max}^m, \quad \forall\, j \in \mathcal{N}_m,\ m \in \mathcal{M}_1, \tag{14}$$

$$N\sum_{j=1}^{n_m}(A_j^m u) + N\rho_m \sum_{j=1}^{n_m}(A_j^m u)^2 \le n_m \mathrm{BED}_{\mathrm{mean}}^m, \quad m \in \mathcal{M}_2, \tag{15}$$

$$\sum_{j=1}^{n_m} f_j^m(N,u) \le K_m, \quad m \in \mathcal{M}_3, \tag{16}$$

$$Su \le 0, \tag{17}$$

$$u \ge 0, \tag{18}$$

$$1 \le N \le N_{\max}, \quad \text{integer}. \tag{19}$$

This formulation includes all constraints that are essential for capturing the tradeoff between tumor BE and the BED for serial and parallel normal tissue. Additional constraints can be added to this formulation if required by the treatment protocol. For instance, a minimum dose constraint on tumor could be easily added to avoid cold spots; similarly, a maximum dose constraint on tumor could be added to increase dose uniformity. Being linear, these constraints pose no additional computational hurdles. Moreover, they might make our formulation more relevant for clinical practice. We decided, however, not to include them in the formulation for three reasons: (i) they would be a deviation from the central theme of existing research on optimal fractionation—that of maximizing tumor BE subject to BED upper limits on normal tissues; (ii) in our preliminary numerical experiments, we observed that the qualitative trends discovered in our sensitivity analyses continue to hold even when these constraints are included; and (iii) our smoothness constraints at least to some extent attempt to ensure dose uniformity.

Observe that for each fixed N, the functions $f_j^m(N,u)$ are discontinuous in u. In fact, it is well known in the IMRT literature that dose-volume constraints are difficult to handle (Romeijn et al. 2006). In realistic instances of [P], the number of beamlets k is likely to equal a few thousand. The number of constraints can also be in the tens or hundreds of thousands, depending on the total number of normal tissue voxels. As a result, exact solution of [P] is computationally intractable. We next develop an algorithm for the efficient, approximate solution of [P]. This method uses a simple constraint-generation approach that is rooted in the fact that when N is fixed, if we drop the dose-volume constraints, then the resulting problem, although seemingly nonconvex, can be equivalently rewritten with a linear objective and convex, quadratic constraints. We emphasize here that if the treatment protocol does not include any dose-volume constraints, then our method produces an exact solution to [P].

3. An Efficient Solution Method

We first define a sequence of problems [P(N)], obtained by fixing N at $1, 2, \ldots, N_{\max}$ in [P]. We have

$$[\mathrm{P}(N)] \quad F^*(N) = \max_u \{N\alpha_0(\bar{A}u) + N\beta_0(\bar{A}u)^2\}, \tag{20}$$

$$\text{subject to (14)–(18)}. \tag{21}$$

Note that

$$F^* = \max_{N \in \{1,2,\ldots,N_{\max}\}} \{F^*(N) - \tau(N)\}. \tag{22}$$

Thus, problem [P] can be solved by first solving the sequence of problems [P(N)], for $N = 1, 2, \ldots, N_{\max}$, and then choosing an N that yields the best tumor BE and using the corresponding optimal fluence map. It is established in Appendix A that [P(N)] has an optimal solution for each N; this implies that [P] has an optimal solution as well. This approach could be seen as spatiotemporal optimization in two steps: (20)–(21) handles only the spatial component and (22) tackles only the temporal component, with both problems employing the biological objective of tumor BE. Note, however, that an optimal fluence map $u^*(N)$ for (20)–(21) depends explicitly on N. In contrast, this was not the case in our separated method in Saberian et al. (2016), where the fluence-map was not a decision variable and in particular did not depend on N. We therefore call our work here a *spatiotemporally integrated approach*.

We recall that in our earlier work in Saberian et al. (2016) on a spatiotemporally separated formulation of the fractionation problem, we were able to prove that the optimal objective value was a quasiconcave function of N. This implied that the optimal number of fractions is the earliest value of N at which the objective drops. This streamlined the search over N somewhat. Unfortunately, we have not been able to prove a similar result for our spatiotemporally integrated formulation. One key difficulty is that the dose-volume constraints (16) render an analysis of the structure of

optimal solutions to [P(N)] as a function of N essentially intractable. Even if these dose-volume constraints were not included in the formulation, [P(N)] does not satisfy standard conditions (Fiacco and Kyparisis 1986, Kyparisis and Fiacco 1987) for quasiconcavity of optimal value function parametric programs. A problem-specific proof can be developed for the very special case of a single normal tissue with maximum dose constraints, but we have not been able to generalize it to other more realistic cases. Consequently, we rely on the above brute force method of finding an optimal solution to [P(N)] for each possible value of N and then pick the best. Fortunately, as we will show next, problem [P(N)] can be approximately solved very efficiently, so we do not see the brute force method as a limitation in practice.

Now observe that because the objective in [P(N)] is increasing in $\bar{A}u$, it is equivalent to maximizing $\bar{A}u$. Thus, we rewrite [P(N)] as

$$[\mathrm{P}(N)'] \quad \max_u \bar{A}u, \tag{23}$$

$$\text{subject to (14)–(18).} \tag{24}$$

Moreover, since $A_j^m u \geq 0$, the maximum dose constraints can be equivalently rewritten as linear constraints wherein the right-hand side is obtained by solving a quadratic equation. This yields the equivalent problem

$$[\mathrm{P}(N)''] \quad \max_u \bar{A}u, \tag{25}$$

$$\text{subject to}$$

$$A_j^m u \leq \frac{-1+\sqrt{1+4\rho_m \mathrm{BED}_{\max}^m/N}}{2\rho_m}, \quad \forall\, j \in \mathcal{N}_m,\ m \in \mathcal{M}_1, \tag{26}$$

$$\text{(15)–(18).} \tag{27}$$

The objective function in this problem is linear; most constraints are either linear or convex quadratic. Thus, the only remaining computational challenge is posed by the dose-volume constraints. We therefore propose a simple and natural constraint-generation approach to surmount this difficulty. In particular, we first solve [P(N)''] *without* dose-volume constraints. Suppose $\hat{u}$ is an optimal solution to this problem. Then for each $m \in \mathcal{M}_3$, we find $n_m - K_m$ voxels that receive the smallest doses among the n_m voxels in O_m under fluence map $\hat{u}$. Let subset $\mathcal{N}_m(\hat{u}, N) \subseteq \mathcal{N}_m$ denote this group of voxels. We then re-solve [P(N)''] but this time by replacing the dose-volume constraints with tolerance limits on all voxels in the set $\mathcal{N}_m(\hat{u}, N)$. Finally, we note that these tolerance limits, which appeared in definition (11) of functions $f_j(u, N)$, can be equivalently rewritten as linear constraints whose right-hand sides are obtained by solving a quadratic equation. This yields the problem

$$[Q(N)] \quad G^*(N) \triangleq \max_u \bar{A}u, \tag{28}$$

$$\text{subject to (14), (15),} \tag{29}$$

$$A_j^m u \leq \frac{-1+\sqrt{1+4\rho_m \mathrm{BED}_{\mathrm{dv}}^m/N}}{2\rho_m}, \quad \forall\, j \in \mathcal{N}_m(\hat{u}, N),\ m \in \mathcal{M}_3, \tag{30}$$

$$\text{(17)–(18).} \tag{31}$$

Problem [$Q(N)$] has a linear objective and only includes linear or convex quadratic constraints; hence it can be solved efficiently. We conclude this section by summarizing our overall algorithm for approximate solution of [P].

Algorithm for solving [P]

1. For $N = 1, 2, \ldots, N_{\max}$

(a) Solve problem [P(N)''] *without* dose-volume constraints; let $\hat{u}$ denote a fluence map that is optimal to this problem, and let $\mathcal{N}_m(\hat{u}, N)$, for each $m \in \mathcal{M}_3$, be the set of voxels that receive the smallest doses among the n_m voxels in O_m under Fluence map $\hat{u}$.

(b) Solve problem [$Q(N)$] to denote its optimal solution by $u^*(N)$ and use its optimal value $G^*(N)$ to approximate the optimal value $F^*(N)$ as $F^*(N) \approx \bar{F}(N) \triangleq N\alpha_0 G^*(N) + N\beta_0 (G^*(N))^2$;

end the loop over N.

2. Use $\bar{F}(N)$ as an approximation to $F^*(N)$ in (22) to obtain an optimal number of fractions N^* and use the corresponding optimal fluence map $u^*(N^*)$ in each fraction.

In Section 4, we apply this algorithm to 10 test cases in head-and-neck and prostate cancer. We perform sensitivity analyses and also quantify the potential benefit of our spatiotemporally integrated approach.

4. Results

In this section, our computational experiments are designed to illustrate two key Points. First, the qualitative trends in the effect of various problem parameters on the optimal number of fractions and the corresponding optimal tumor BE are identical to those in our recent spatiotemporally separated model (Saberian et al. 2016) and also to those in some of the earlier stylized models (Armpilia et al. 2004; Bortfeld et al. 2015; Fowler 1990, 2001, 2007, 2008; Fowler and Ritter 1995; Jones et al. 1995; Keller et al. 2012; Mizuta et al. 2012; Unkelbach et al. 2013b). Second, crucially, the spatiotemporally integrated approach achieves a higher tumor BE than both a model that uses a spatially optimized IMRT fluence map without optimizing the number of fractions and our spatiotemporally separated model in Saberian et al. (2016). The first of these two points is studied in Section 4.2; it serves as an indirect validation of our model. The second point, studied in Section 4.3, hints at the potential increase in treatment efficacy, within the LQ framework that could be obtained by solving our integrated model instead of solving existing stylized models in the literature.

Table 2. Description of the Geometry Used in Head-and-Neck Cancer Cases

Case	No. of beamlets (k)	No. of tumor voxels (n)	No. of normal tissues voxels
1	3,910	27,576	67,386
2	3,888	31,930	67,270
3	4,128	36,320	76,160
4	3,003	22,372	53,176
5	3,256	28,638	64,713

Note. These data are identical to Saberian et al. (2016).

Table 3. Tolerance Doses for Various Normal Tissues in Head-and-Neck Test Cases Where the Dose Is Administered in $N_{conv} = 35$ Equal-Dose Fractions

Normal tissue	D_{max} (Gy)	D_{mean} (Gy)	D_{dv} (Gy), ϕ
Spinal cord	45	N/A	N/A
Brainstem	50	N/A	N/A
Left and right parotids	N/A	28	N/A
Unspecified normal tissue	77	N/A	70, 0.05

Notes. Recall that for dose-volume type constraints, no more than a volume fraction ϕ of the normal tissue can receive dose more than D_{dv}. This treatment protocol is similar, for example, to Marks et al. (2010).

4.1. Description of Test Cases

We first describe the 10 test cases we used in our experiments. Five were head-and-neck cases and the other five were prostate cases. All test cases were generated using our in-house phantom creator software PhanC written in MATLAB (Saberian and Kim 2014) and are available online at http://faculty.washington.edu/archis/spintfracdata.zip. Dose calculation in PhanC is performed via a tissue-maximum ratio lookup table (see Mayles et al. 2007, Chap. 23). All test cases in this paper are identical to the ones we used in Saberian et al. (2016). These test cases are three dimensional and were carefully developed to be representative of clinical scenarios in terms of geometry and size. Specifically, our test cases were similar to those discussed in Gu et al. (2009), Men et al. (2009), Romeijn et al. (2006), Romeijn and Dempsey (2008), and Salari and Romeijn (2012). All voxels were $3 \times 3 \times 3$ mm^3. The beamlet resolution was 5×5 mm^2 in all cases. All cases used equally spaced coplanar beams (seven for head-and-neck and five for prostate). Computer simulations were performed on a 3.1 GHz iMac desktop with 16 GB RAM using the MATLAB convex optimization toolbox CVX (Grant and Boyd 2009).

4.1.1. Head-and-Neck Cancer Cases.

All cases used seven beams and included spinal cord, brainstem, left and right parotids, and unspecified normal tissue between these critical organs. The total number of voxels in the head-and-neck target and in the normal tissues and the total number of beamlets is shown in Table 2.

The conventional fractionation schedule was assumed to include $N_{conv} = 35$ fractions. While formulating problem [P], we included maximum dose constraints for spinal cord, brainstem, and unspecified normal tissue. A dose-volume constraint for unspecified normal tissue was also added. Mean dose constraints were used for left and right parotids. The tolerance dose values for various normal tissues were similar to Emami et al. (1991), Kehwar (2005), Marks et al. (2010), and Mavroidis et al. (2011) and identical to Saberian et al. (2016). These are listed in Table 3. All radiobiological parameter values used are listed in Table 4, along with their source.

4.1.2. Prostate Cancer Cases.

All cases used five beams and included rectum, bladder, left and right femurs, and unspecified normal tissue between these critical organs. The total number of voxels in the prostate target and in the normal tissues, and the total number of beamlets, is shown in Table 5.

The conventional fractionation schedule was assumed to include $N_{conv} = 45$ fractions. In our formulation of problem [P], we included a maximum dose constraint for unspecified normal tissue and included dose-volume constraints for all normal tissues. There were no mean dose constraints. The dose-volume constraints for all normal tissues were similar to Emami et al. (1991), Kehwar (2005), Marks et al. (2010), and Mavroidis et al. (2011) and identical to Saberian et al. (2016). These are listed in Table 6. All radiobiological parameter values used are listed in Table 7 along with their source.

Table 4. Values of Various Radiobiological Parameters Used in Sensitivity Analyses for Head-and-Neck Cancer

Structure	Parameter	Value(s)	Source
Head-and-neck tumor	α	0.35 Gy^{-1}	Fowler (1990, 2001, 2007, 2008)
	α/β	{8, 10, 12} Gy	Fowler (2007), Qi et al. (2012), Williams et al. (1985)
	T_{double}	{2, 3, 5, 8, 10, 20, 40, 50} days	Fowler (1990, 2007), Qi et al. (2012), Yang and Xing (2005)
	T_{lag}	{7, 14, 21, 28, 35} days	Fowler (2007)
Unspecified normal tissue	α/β	3 Gy	Fowler (1984), Joiner and van der Kogel (2009), Thames et al. (1989)
Parotids	α/β	{3, 4, 5, 6} Gy	Fowler (1990, 2007), Yang and Xing (2005)
Spinal cord and brainstem	α/β	{2, 3, 4, 5, 6} Gy	Fowler (1990, 2007), Yang and Xing (2005)

Table 5. Description of the Geometry Used in Prostate Cancer Cases

Case	No. of beamlets (k)	No. of tumor voxels (n)	No. of normal tissues voxels
1	938	6,180	145,545
2	847	7,225	326,703
3	935	4,628	367,656
4	930	4,956	314,544
5	870	4,840	269,450

Note. These data are identical to Saberian et al. (2016).

Table 6. Dose-Volume Constraints for Various Normal Tissues when Dose is Administered in $N_{conv} = 45$ Equal-Dose Fractions—No More than a Volume Fraction ϕ of the Normal Tissue Can Receive Dose More than D_{dv}

Normal tissue	D_{dv} (Gy), ϕ
Rectum	50, 0.5 85, 0.05
Bladder	50, 0.5 70, 0.35 75, 0.25 80, 0.15 89, 0.05
Femurs	65, 0.05
Unspecified normal tissue	81, 0.05

Note. This treatment protocol is similar, for example, to Marks et al. (2010).

4.2. Sensitivity to Tumor Doubling Time and Time Lag Before Proliferation

As in previous work in this area, we found that the optimal number of fractions is smaller for faster-growing tumors, as characterized by smaller values of the tumor doubling time T_{double}. As an example, the tumor BE is plotted against N for various values of T_{double} in Figures 1(a), (b) for our head-and-neck case 1 and prostate case 1. Also, the optimal tumor BE itself is smaller for faster-growing tumors.

Our simulations showed that the tumor BE can sometimes grow very slowly with N before it starts decreasing. We therefore tracked the smallest number of fractions at which the tumor BE reached 99% of its optimal value. We denote this number of fractions by N^*_{99}. The range[1] of this number over all combinations of tumor α/β ratios and normal tissue α/β ratios for our five head-and-neck cases is reported in Table 8. The table shows that the ranges did not change significantly across different cases. The table also shows that for some fixed values of T_{double}, the range of N^*_{99} is somewhat broad; this is especially true for slower proliferating tumors, as characterized by larger T_{double} values. These broad ranges for N^*_{99} resulted from our choice of a somewhat broad range for α/β values. To further illustrate this point, we present a more detailed set of results for head-and-neck case 1 as an example in Table 9. These results were obtained for $T_{double} =$ 10 days and $T_{lag} = 7$ days by fixing the α/β ratios for the unspecified normal tissue, spinal cord, and brainstem at 3 Gy and then varying the α/β ratios for the two parotids over the set $\{3,4,5,6\}$ Gy and the α/β ratios for the tumor over the set $\{8,10,12\}$ Gy. The table shows that for a fixed value of parotid α/β ratio, N^*_{99} increases with increasing values of tumor α/β. Similarly, for a fixed value of tumor α/β ratio, N^*_{99} decreases with increasing values of parotid α/β. In summary, N^*_{99} becomes larger as the relative difference between tumor and parotid α/β grows.

In all prostate cases where the tumor α/β ratio was 2 or 3, it was optimal to administer a single fraction for all combinations of α/β ratios for normal tissues, as has been noted in the literature on stylized models. The range of N^*_{99} for all combinations of α/β ratios for normal tissues and $\alpha/\beta = 4,6$ for tumors is shown in Table 10 for our five test cases. The table shows that the ranges did not change significantly across different cases. To shed further light on the somewhat broad range of N^*_{99} values for some fixed values of T_{double}, we present more detailed results for prostate case 1 as an example in Table 11. These results were obtained by fixing $T_{double} = 30$ days and $T_{lag} = 7$ days, fixing the unspecified normal tissue and femur α/β at 3 Gy,

Table 7. Values of Various Radiobiological Parameters Used in Sensitivity Analyses for Prostate Cancer

Structure	Parameter	Value (s)	Source
Prostate tumor	α	0.15 Gy^{-1}	Fowler (1990, 2001, 2007, 2008)
	α/β	$\{2,3,4,6\}$ Gy	Brenner and Hall (1999), Fowler et al. (2001), Fowler and Ritter (1995), Wang et al. (2003)
	T_{double}	$\{5,20,40,60,80\}$ days	Fowler et al. (2001), Fowler and Ritter (1995), Gao et al. (2010), Haustermans et al. (1997)
	T_{lag}	$\{7,14,21,28,35\}$ days	Gao et al. (2010), Haustermans et al. (1997)
Unspecified normal tissue	α/β	3 Gy	Fowler (1984), Joiner and van der Kogel (2009), Thames et al. (1989)
Femurs	α/β	$\{3,4,5,6\}$ Gy	Brenner (2004), Fowler and Ritter (1995), Joiner and van der Kogel (2009)
Rectum and bladder	α/β	$\{3,4,5,6\}$ Gy	Brenner (2004), Fowler and Ritter (1995), Joiner and van der Kogel (2009), Marzi et al. (2009)

Figure 1. (Color Online) Sensitivity of the Optimal Number of Fractions and the Optimal Tumor BE to Tumor Doubling Time T_{double} (Days) When $T_{\text{lag}} = 7$ Days

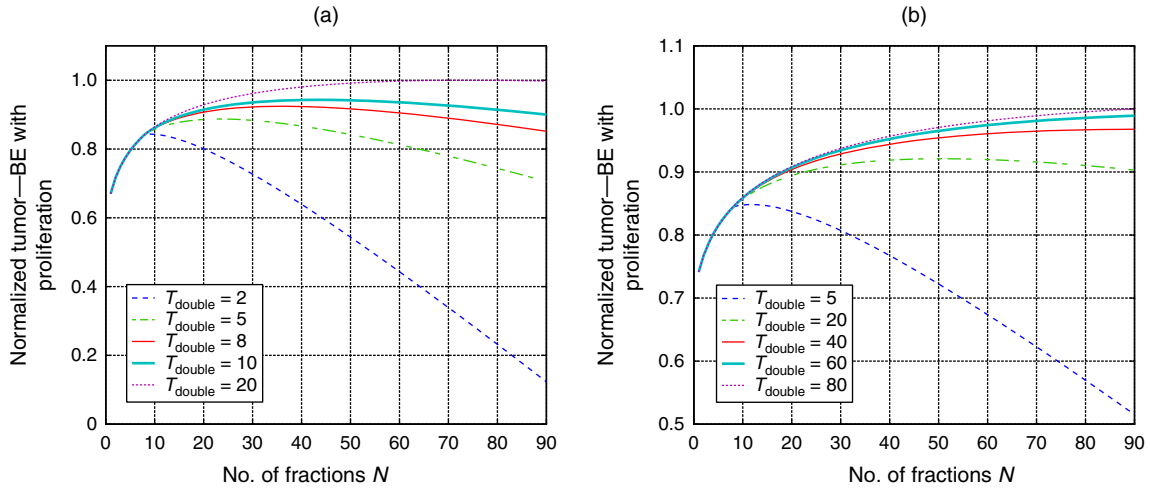

Notes. (a) Head-and-neck case 1: tumor α/β was 10 Gy, and the α/β ratio for all normal tissues was 3 Gy. (b) Prostate case 1: tumor α/β was 6 Gy, and the α/β ratio for all normal tissues was 3 Gy.

varying the bladder and rectum α/β ratios over the set $\{3, 4, 5, 6\}$ Gy, and varying the tumor α/β ratio over the set $\{4, 6\}$ Gy. As in head-and-neck cancer, N^*_{99} increases with increasing relative difference between tumor and normal tissue α/β.

We also investigated the sensitivity of the optimal number of fractions to T_{lag}. Our experiments confirmed (see Tables 12 and 13) that for small values of T_{double} relative to T_{lag}, the optimal number of fractions is equal to $1 + T_{\text{lag}}$; for larger values of T_{double}, the optimal number of fractions is not sensitive to T_{lag}. As in Tables 8 and 10, the range of N^*_{99} did not vary across different test cases; therefore, in Tables 12 and 13, we simply listed the range of N^*_{99} over all head-and-neck and prostate cases, respectively, rather than separating them case by case. For each T_{double}, T_{lag} combination, the somewhat broad range of N^*_{99} again resulted from our broad range of α/β values, as previously demonstrated in Tables 9 and 11.

4.3. Improvement in Tumor BE

4.3.1. Comparison with Conventional IMRT. First, we compare the tumor BE obtained by our spatiotemporally integrated approach with that from a conventional

Table 8. Range of N^*_{99} Across Five Head-and-Neck Cases with $T_{\text{lag}} = 7$ Days and All Combinations of Tumor and Normal Tissue α/β Ratios

	T_{double} (days)							
Case	2	3	5	8	10	20	40	50
1	8	8–11	8–19	10–28	12–33	23–55	38–73	44–75
2	8	8–13	9–22	15–33	19–39	34–63	52–76	58–78
3	8	8–13	9–22	15–32	18–38	32–63	52–76	58–78
4	8	8–12	8–20	13–30	16–36	29–59	49–75	55–77
5	8–9	8–14	10–22	16–34	20–40	36–64	55–77	60–78

Table 9. Range of N^*_{99} for Head-and-Neck Case 1 with $T_{\text{double}} = 10$ Days, $T_{\text{lag}} = 7$ Days, and Different Combinations of Tumor and Parotid α/β Ratios with α/β for Unspecified Normal Tissue, Spinal Cord, and Brainstem Fixed at 3 Gy

	Tumor α/β		
Parotid α/β	8	10	12
3	22	29	33
4	18	25	30
5	15	22	27
6	12	20	25

Table 10. Range of N^*_{99} for Five Prostate Cases with $T_{\text{lag}} = 7$ Days and $\alpha/\beta = 4, 6$ for Tumor and All Combinations of Normal Tissue α/β Ratios

	T_{double} (days)							
Case	5	8	10	20	30	40	60	80
1	8	8–12	8–16	8–31	8–44	8–56	8–68	8–72
2	8	8–12	8–16	8–32	8–46	8–58	8–69	8–73
3	8	8–11	8–15	8–30	8–43	8–54	8–67	8–71
4	8	8–12	8–16	8–32	8–46	8–57	8–68	8–72
5	8	8–12	8–16	8–32	8–46	8–58	8–69	8–73

Table 11. Range of N^*_{99} for Prostate Case 1 with $T_{\text{double}} = 30$ Days, $T_{\text{lag}} = 7$ Days, and Different Combinations of Tumor, Rectum, and Bladder α/β Ratios with α/β for Unspecified Normal Tissue and Femurs Fixed at 3 Gy

	Tumor α/β	
Rectum and bladder α/β	4	6
3	8	44
4	8	26
5	8	20
6	8	18

Table 12. Range of N^*_{99} over Five Head-and-Neck Cases Across All Combinations of Tumor and Normal Tissue α/β Ratios

	T_{double} (days)							
T_{lag} (days)	2	3	5	8	10	20	40	50
14	15	15	15–22	15–33	15–40	22–64	38–76	44–78
21	22	22	22	22–33	22–40	22–64	38–76	44–78
28	29	29	29	29	29–33	29–55	38–73	44–75
35	36	36	36	36	36	36–55	38–73	44–75

Table 13. Range of N^*_{99} over Five Prostate Cases for $\alpha/\beta = 4, 6$ for Tumor Across All Combinations of Normal Tissue α/β Ratios

	T_{double} (days)							
T_{lag} (days)	5	8	10	20	30	40	60	80
14	8–15	10–15	8–16	8–32	10–46	8–58	10–69	8–73
21	8–22	8–22	8–22	8–32	10–46	10–58	10–69	8–73
28	8–29	8–29	8–29	8–32	8–46	8–58	8–69	8–73
35	8–36	8–36	8–36	8–36	8–45	8–57	8–69	8–73

IMRT optimization model that does not optimize the number of fractions. The number of fractions and the prescription dose were fixed at $N_{\text{hn}} = 35$, $D_{\text{hn}} = 70$ Gy for head-and-neck cancer, and $N_{\text{pr}} = 45$, $D_{\text{pr}} = 81$ Gy for prostate cancer similar to Marks et al. (2010). The IMRT optimization model minimized the total squared-deviation of tumor voxel doses from the prescription doses. Maximum dose constraints for spinal cord and brainstem and mean dose constraints for parotids with dose tolerance levels tabulated in Section 4.1.1 were included for head-and-neck cases. Maximum dose constraints of 85, 89, and 65 Gy for rectum, bladder, and femurs, respectively, were included for the prostate cases, similar to Marks et al. (2010). Smoothness constraints were included in all 10 cases.

For head-and-neck cases, we use superscripts/subscripts 0, 1, 2, 3, and 4 to represent dose-deposition matrices, tolerance doses, voxel sets, and number of voxels for the tumor, spinal cord, brainstem, left parotid, and right parotid, respectively. The resulting model for head and neck was as follows:

$$\begin{aligned}
[\text{HN-CONV}] \quad & \min \sum_{i=1}^{n_0} |A_i^0 u - D_{\text{hn}}/N_{\text{hn}}|^2 \\
& N_{\text{hn}} A_j^1 u \le D_{\max}^1, \quad j \in \mathcal{N}^1, \\
& N_{\text{hn}} A_j^2 u \le D_{\max}^2, \quad j \in \mathcal{N}^2, \\
& N_{\text{hn}} \sum_{j=1}^{n_3} A_j^3 u \le n_3 D_{\text{mean}}^3, \\
& N_{\text{hn}} \sum_{j=1}^{n_4} A_j^4 u \le n_4 D_{\text{mean}}^4, \\
& Su \le 0, \\
& u \ge 0.
\end{aligned}$$

Suppose u^{hn} is an optimal solution to this problem. Then its tumor BE is computed using formula (2) as

$$N_{\text{hn}}\alpha_0(\bar{A}^0 u^{\text{hn}}) + N_{\text{hn}}\beta_0(\bar{A}^0 u^{\text{hn}})^2 - \tau(N_{\text{hn}}).$$

For prostate cases, we use superscripts/subscripts 0, 1, 2, 3, and 4 to represent dose-deposition matrices, tolerance doses, voxel sets, and number of voxels for the tumor, rectum, bladder, left femur, and right femur, respectively. The model for prostate was as follows:

$$\begin{aligned}
[\text{PR-CONV}] \quad & \min \sum_{i=1}^{n} |A_i^0 u - D_{\text{pr}}/N_{\text{pr}}|^2 \\
& N_{\text{pr}} A_j^1 u \le D_{\max}^1, \quad j \in \mathcal{N}^1, \\
& N_{\text{pr}} A_j^2 u \le D_{\max}^2, \quad j \in \mathcal{N}^2, \\
& N_{\text{pr}} A_j^3 u \le D_{\max}^3, \quad j \in \mathcal{N}^3, \\
& N_{\text{pr}} A_j^4 u \le D_{\max}^4, \quad j \in \mathcal{N}^4, \\
& Su \le 0, \\
& u \ge 0.
\end{aligned}$$

Suppose u^{pr} is an optimal solution to this problem. Then its tumor BE is computed using formula (2) as

$$N_{\text{pr}}\alpha_0(\bar{A}^0 u^{\text{pr}}) + N_{\text{pr}}\beta_0(\bar{A}^0 u^{\text{pr}})^2 - \tau(N_{\text{pr}}).$$

The improvements in tumor BE obtained by our spatiotemporally integrated approach over conventional IMRT are listed in Figures 2(a) and (b) for head-and-neck and prostate cancer, respectively, for $T_{\text{lag}} = 7$ days as an example since the trends in improvements were not sensitive to T_{lag}.

Figure 2(a) for head-and-neck cases shows that the improvement in tumor BE achieved by our spatiotemporally integrated approach over conventional IMRT first decreases and then increases with increasing values of T_{double}. Specifically, the potential benefit of our integrated approach is likely to be the largest for fast and slowly proliferating head-and-neck tumors. In particular, the most significant benefits are likely to be achieved for fast proliferating tumors. This overall trend is consistent with the fact that the optimal number of fractions obtained by our integrated approach is closest to the conventional value of 35 for moderately proliferating tumors, as seen in Table 8.

Figure 2(b) for prostate cases shows a different trend. For each case, the improvement decreases with increasing values of T_{double}. The magnitude of the improvement itself seems to be bigger than that in head-and-neck cases. This is because, as seen in Table 10, the optimal number of fractions is significantly different from the conventional value of 45 for most parameter combinations.

A more detailed analysis of the trends in Figures 2(a) and 2(b) is provided in Figures 3(a) and 3(b) for head-and-neck case 1 and prostate case 1, respectively. For

Figure 2. (Color online) Average Percentage Improvement Achieved by Our Spatiotemporally Integrated Approach (a) IMRT for head-and-neck; (b) IMRT for prostate; (c) Spatiotemporally separated model in Saberian et al. (2016) for head and neck; (d) Spatiotemporally separated model in Saberian et al. (2016)

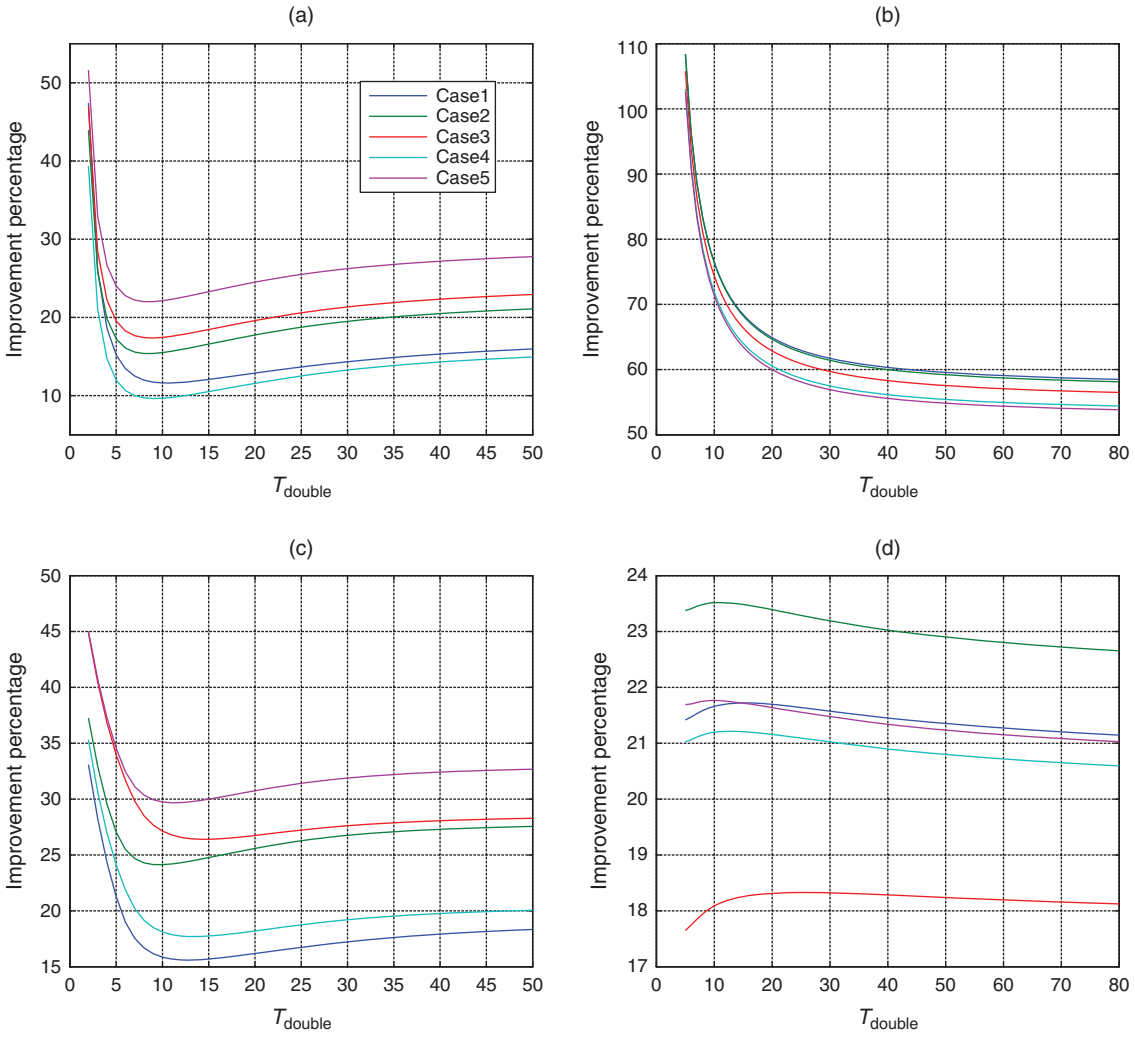

Note. These numbers are for $T_{\text{lag}} = 7$ days and averaged over all combinations of tumor and normal tissue α/β ratios.

Figure 3. (Color Online) Average Percentage Improvement Achieved by Our Spatiotemporally Integrated Approach over IMRT (a) Head-and-neck case 1; (b) Prostate case 1

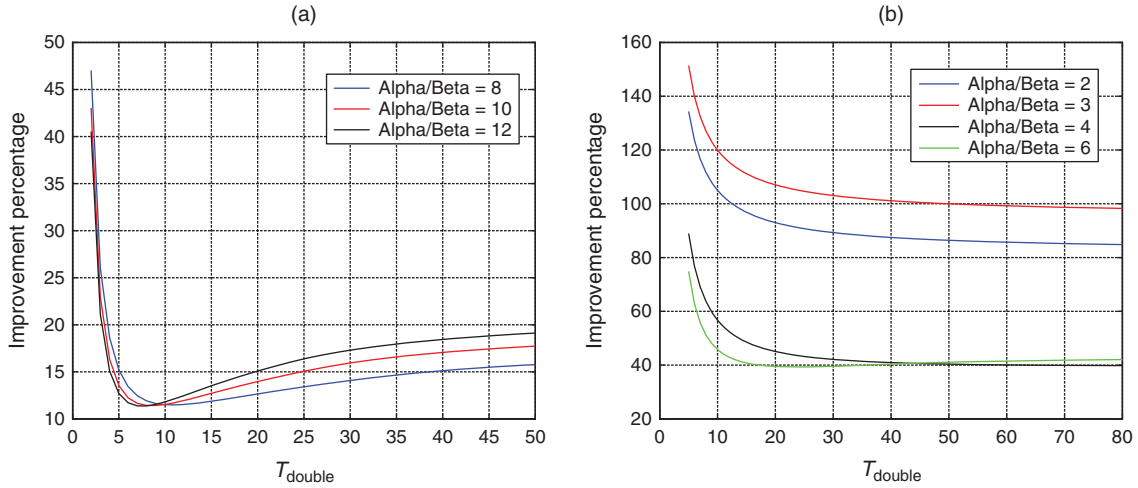

Note. These numbers are for $T_{\text{lag}} = 7$ days with all normal tissue α/β ratios fixed at 3 for different tumor α/β ratios.

head-and-neck cases, Figure 3(a) shows that, for most values of T_{double}, the spatiotemporally integrated model achieves larger improvements over conventional IMRT for larger values of tumor α/β when all normal tissue α/β ratios are fixed at 3 Gy. This is because the difference between the optimal number of fractions derived from our integrated model and the conventional value of 35 increases for larger values of tumor α/β. For the prostate case, Figure 3(b) shows that the largest improvement is achieved when tumor α/β is 2 or 3 Gy when all normal tissue α/β ratios are fixed at 3 Gy. This is because, as stated earlier, a single fraction is optimal in those cases and this value is significantly different from the conventional value of 45.

4.3.2. Comparison with a Spatiotemporally Separated Model. Second, we compare the tumor BE achieved by our spatiotemporally integrated model with that attained by our spatiotemporally separated model in Saberian et al. (2016). In that model, the objective was to maximize the BE of average tumor dose subject to the same dose constraints on normal tissues as in our formulation [P]. However, there a spatially optimized IMRT fluence map as in Section 4.3.1 was assumed to be available as input and fixed a priori; the number of fractions was then optimized with respect to this fluence map using a sparing factors approach. This led to a closed-form formula for the average tumor dose per fraction as a function of the number of fractions. The tumor BE of this average tumor dose was then characterized as a quasiconcave function of the number of fractions using formula (2). This resulted in a simple procedure for finding an optimal number of fractions.

The improvements in tumor BE obtained by our spatiotemporally integrated approach over the spatiotemporally separated model are plotted in Figures 2(c) and 2(d) for head-and-neck and prostate cases, respectively, for $T_{\text{lag}} = 7$ days as an example. The qualitative trend in the improvements shown in Figure 2(c) for our head-and-neck cases is similar to that in Figure 2(a). For the prostate cases plotted in Figure 2(d), the improvement is much less sensitive to T_{double} since the optimal number of fractions obtained by our integrated approach and the separated model is similar in most cases as this number is often 1 or $1 + T_{\text{lag}}$.

We conclude this section by elaborating on one observation that might seem surprising at first. A comparison of Figures 2(a) and 2(c) shows that the improvement achieved by our spatiotemporally integrated approach over the spatiotemporally separated approach is sometimes larger than that over conventional IMRT. This seems counterintuitive, because the spatiotemporally separated model uses a conventional, spatially optimized IMRT fluence map for a conventional number of fractions as input and improves on it by optimizing the number of fractions. Specifically, the improvement over IMRT should be at least as large as the improvement over the spatiotemporally separated model. This intuition is correct. The apparent contradiction is rooted in the fact that the constraints in our spatiotemporally separated model in Saberian et al. (2016) were more conservative than in the conventional IMRT model used here. This is because, for reasons explained in Section 2.2.2, the spatiotemporally separated model in Saberian et al. (2016) also puts an upper bound on the average BED over all normal tissue voxels, as in this paper, whereas conventional IMRT uses an upper bound on the average dose over all voxels.

4.4. Effect of Minimum and Maximum Tumor Dose Constraints

Our formulation [P] does not explicitly include minimum or maximum dose constraints on the tumor. The absence of minimum dose constraints may lead to tumor doses that are lower than those administered by the conventional IMRT plan in some voxels, which is clinically undesirable. One way to address this is to add constraints to force tumor BED in all voxels to be at least as large as that of conventional IMRT. However, this is likely to reduce the BE of the average tumor dose. We therefore studied this loss in our objective function value by adding such minimum tumor BED constraints to $[P(N^*)]$ for $T_{\text{double}} = 5, 10, 20$ (days), $T_{\text{lag}} = 7$ (days), tumor $\alpha/\beta = 10$ Gy, and normal tissue $\alpha/\beta = 3$ Gy. Table 14 shows that this loss is clinically insignificant in most cases.

We also investigated the improvement in tumor BE attained by our method in the presence of maximum dose constraints on the tumor along with minimum dose constraints, over conventional IMRT. In this sensitivity analysis, we kept the minimum dose constraints on $[P(N^*)]$ as above and included maximum dose constraints at various levels. The right-hand side of the maximum dose constraint was set to equal 20%–40% above the prescription dose from conventional IMRT in BED equivalents. In addition, as an extreme case, we studied the improvement in tumor BE in $[P(N^*)]$

Table 14. Percentage Improvement in Tumor BE Attained by Our Method "Without" and "With" Minimum Tumor Dose Constraints Over Conventional IMRT

Head-and-neck case	T_{double} (days) (%)					
	5		10		20	
	Without	With	Without	With	Without	With
1	15	14	12	9	15	10
2	17	17	16	16	19	19
3	20	19	19	17	21	20
4	12	11	10	9	13	12
5	24	24	23	21	26	26

Note. These results are for $T_{\text{lag}} = 7$ (days), tumor $\alpha/\beta = 10$ Gy, and normal tissue $\alpha/\beta = 3$ Gy.

Table 15. Percentage Improvement in Tumor BE Attained by Our Approach "Without" Minimum/Maximum Dose Constraints, and with Minimum/Maximum Dose Constraints on the Tumor, over Conventional IMRT

Head-and-neck case	Without (%)	Maximum constraints (%)			
		$1.4 \times D_{hn}$	$1.3 \times D_{hn}$	$1.2 \times D_{hn}$	Matched
1	15	14	13	11	3
2	17	15	13	10	7
3	20	17	15	11	8
4	12	11	10	8	5
5	24	21	19	14	11

Notes. Column headings $1.4 \times D_{hn}$, $1.3 \times D_{hn}$, and $1.2 \times D_{hn}$ mean that the right-hand side of the maximum dose constraint was 40%, 30%, and 20%, respectively, over the prescription dose D_{hn} for conventional IMRT in BED equivalents. For the "matched" column, the minimum and maximum dose constraint levels were set to exactly equal those from the conventional IMRT plans in BED equivalents. These results are for $T_{double} = 5$ (days), $T_{lag} = 7$ (days), tumor $\alpha/\beta = 10$ Gy, and normal tissue $\alpha/\beta = 3$ Gy.

Table 16. Percentage Improvement in Tumor BE Attained by Our Approach "Without" Minimum/Maximum Dose Constraints, and with Minimum/Maximum Dose Constraints on the Tumor, over Conventional IMRT

Head-and-neck case	Without (%)	Maximum constraints (%)			
		$1.4 \times D_{hn}$	$1.3 \times D_{hn}$	$1.2 \times D_{hn}$	Matched
1	12	9	8	7	2
2	16	14	12	9	8
3	19	15	13	9	8
4	10	9	8	7	5
5	23	19	16	12	11

Notes. Column headings $1.4 \times D_{hn}$, $1.3 \times D_{hn}$, and $1.2 \times D_{hn}$ mean that the right-hand side of the maximum dose constraint was 40%, 30%, and 20%, respectively, over the prescription dose D_{hn} for conventional IMRT in BED equivalents. For the "matched" column, the minimum and maximum dose constraint levels were set to exactly equal those from the conventional IMRT plans in BED equivalents. These results are for $T_{double} = 10$ (days), $T_{lag} = 7$ (days), tumor $\alpha/\beta = 10$ Gy, and normal tissue $\alpha/\beta = 3$ Gy.

in the presence of minimum and maximum dose constraints with levels exactly equal to those from our conventional IMRT plans. The results are presented in Tables 15–17 for $T_{double} = 5$, 10, and 20 days, respectively. The tables show that our approach improves tumor BE in all cases.

5. Discussion

We built a spatiotemporally integrated model for the optimal fractionation problem using the LQ framework. Decision variables in this formulation correspond to the number of fractions as well as the fluence map. We proposed an efficient, convex programming algorithm for approximate solution of this problem. Computer simulations on test cases suggest that this approach could potentially increase the tumor BE within the LQ framework, compared to a conventional

Table 17. Percentage Improvement in Tumor BE Attained by Our Approach "Without" Minimum/Maximum Dose Constraints, and with Minimum/Maximum Dose Constraints on the Tumor, over Conventional IMRT

Head-and-neck case	Without (%)	Maximum constraints (%)			
		$1.4 \times D_{hn}$	$1.3 \times D_{hn}$	$1.2 \times D_{hn}$	Matched
1	15	10	10	8	2
2	19	16	14	10	9
3	21	18	15	11	10
4	13	12	11	9	6
5	26	23	20	15	13

Notes. Column headings $1.4 \times D_{hn}$, $1.3 \times D_{hn}$, and $1.2 \times D_{hn}$ mean that the right-hand side of the maximum dose constraint was 40%, 30%, and 20%, respectively, over the prescription dose D_{hn} for conventional IMRT in BED equivalents. For the "matched" column, the minimum and maximum dose constraint levels were set to exactly equal those from the conventional IMRT plans in BED equivalents. These results are for $T_{double} = 20$ (days), $T_{lag} = 7$ (days), tumor $\alpha/\beta = 10$ Gy, and normal tissue $\alpha/\beta = 3$ Gy.

IMRT optimization model that does not optimize the number of fractions, and also compared to a recently proposed model that separates the spatial and the temporal components of the problem. Our sensitivity analyses provided insights into the effect of various model parameters on the resulting solutions.

Throughout this paper, and in our previous work in Saberian et al. (2016), we employed the BE of the average dose delivered to different tumor voxels as the objective function. As discussed toward the end of Section 2.1, perhaps the average BE of doses delivered to different tumor voxels would be a clinically more meaningful (although computationally intractable) metric. It may therefore be of some interest to measure and compare the average BE of a treatment plan that optimizes the BE of the average tumor dose. Although we did not report such average BE numbers in this paper, we did calculate them for some representative scenarios in our preliminary work. We emphasize the reassuring observation that the qualitative trends in these average BE numbers were identical to what we reported in this paper for the BE of the average dose. Moreover, the improvements in average BE were also similar to those reported here.

Our algorithm tackles dose-volume constraints in a simple, natural, and efficient manner while preserving convexity. It should also be possible to use other existing methods to handle dose-volume constraints, although we did not pursue this (see, for example, the literature review and methods in Romeijn et al. 2006). We believe that the qualitative observations in this paper will hold for such alternative formulations.

Many alternative fractionation schedules have been tested clinically. Examples include once-daily treatment but only over weekdays and twice-daily treatment only over weekdays. Our formulation [P] can

be easily modified to accommodate such fractionation strategies by redefining function $\tau(N)$ in Equation (1), as described in our previous work in Saberian et al. (2016).

Finally, one limitation of our formulation is the assumption that an identical Fluence map is used in every session; that is, it only considers equal-dosage fractionation. This is consistent with prevalent practice. However, it has been recently suggested in Saberian et al. (2015) and Unkelbach et al. (2013a) that this may not be optimal. It would be interesting to formulate and solve a more general version of our spatiotemporally integrated model that allows the fluence map to change across sessions. The number of variables in such a model will be an order of magnitude larger than that in our model here. We therefore defer the development of efficient algorithms for its approximate solution to future research.

Finally, our previous work in Kim et al. (2012) focused on incorporating biological information acquired from functional images to optimally adapt fluence maps over the treatment course with a fixed number of fractions. It did not focus on optimal fractionation. That model accounted for the uncertainty in tumor response using stochastic control. Our future research will extend that work to optimal fractionation in such a stochastic setting.

Appendix. Proof of Existence of an Optimal Solution to [P(N)]

Without loss of generality, we assume that for every normal tissue $m \in \mathcal{M}$, every row of the dose deposition matrix A^m has at least one strictly positive entry. If not, then the normal tissue voxel corresponding to a zero row in A^m can be removed from further consideration, as radiation does not reach that voxel. Also without loss of generality, we assume that there exists either a serial normal tissue $m \in \mathcal{M}_1$ or a parallel normal tissue $m \in \mathcal{M}_2$ with the property that every column of its dose deposition matrix A^m includes at least one strictly positive entry. If there exists a column c without any strictly positive entries, then the cth component of u, denoted u_c, can be increased arbitrarily without damaging any normal tissue. This assumption is met in practice, for example, when maximum dose constraints are included on the unspecified normal tissue, because each radiation beamlet must pass through at least some unspecified normal tissue and hence the corresponding row of A^m will have a strictly positive entry.

Lemma 1. *Problem* [P(N)] *has an optimal solution for each* $N \geq 1$.

Proof. For every $m \in \mathcal{M}_3$, the dose-volume constraints imply that the BED for at least $L_m \triangleq n_m - K_m$ and at most n_m voxels in O_m should be less than BED^m_{dv}. As a result, there are $W_m = \sum_{l=L_m}^{n_m} \binom{n_m}{l}$ ways to express a dose-volume constraint. Each of these enforces that some combination of $L_m \leq l \leq n_m$ out of the n_m voxels in O_m satisfies the appropriate BED limit. We index these distinct ways by $w_m = 1, 2, \ldots, W_m$ and let $\mathcal{J}_{w_m}(N) \subseteq \mathcal{N}_m$ be the set of voxels in O_m for which the dose limit is enforced in the w_mth way of expressing the dose-volume constraint for O_m. Thus, there are a total of $W = \prod_{m \in \mathcal{M}_3} W_m$ ways to express our dose-volume constraints. Let $\vec{w} \triangleq (w_1, w_2, \ldots, w_{|\mathcal{M}_3|})$. We create W subproblems from [P(N)], each representing one of these W ways of expression:

$$[\text{P}(\vec{w};N)] \quad \max_{\vec{u}(N)} \{N\alpha_0(\bar{A}u) + N\beta_0(\bar{A}u)^2\}, \tag{A.1}$$

$$N(A^m_j u) + N\rho_m(A^m_j u)^2 \leq \text{BED}^m_{\max}, \quad \forall\, j \in \mathcal{N}_m,\ m \in \mathcal{M}_1, \tag{A.2}$$

$$N\sum_{j=1}^{n_m}(A^m_j u) + N\rho_m \sum_{j=1}^{n_m}(A^m_j u)^2 \leq n_m \text{BED}^m_{\text{mean}}, \quad m \in \mathcal{M}_2, \tag{A.3}$$

$$N(A^m_j u) + N\rho_m(A^m_j u)^2 \leq \text{BED}^m_{\text{dv}}, \quad j \in \mathcal{J}_{w_m}(N),\ m \in \mathcal{M}_3, \tag{A.4}$$

$$Su \leq 0, \tag{A.5}$$

$$u \geq 0. \tag{A.6}$$

An optimal solution to [P(N)] can be recovered by choosing the best among optimal solutions to these subproblems. Thus, we prove that each of the above W problems has an optimal solution. Let $U(\vec{w};N) \subset \mathfrak{R}^k$ denote the set of feasible fluence map vectors u. This set is nonempty because the trivial fluence map $u = \vec{0}$ is feasible to [P($\vec{w};N$)]. Suppose a serial normal tissue $m \in \mathcal{M}_1$ has a strictly positive entry in each column of its dose deposition matrix A^m (if a parallel normal tissue possesses this property instead, then the proof can be modified easily). For any $l = 1, 2, \ldots, k$, let $\mathcal{I}_l$ denote the set of rows of A^m in which the entry in the lth column is strictly positive. For all $i \in \mathcal{I}_l$, we denote the corresponding positive entries of A^m by $A^m_{i,l}$. Since all entries in A^m are nonnegative, the maximum dose constraint on this normal tissue implies that $A^m_{i,l} u_l \leq \text{BED}^m_{\max}$ for $t = 1, 2, \ldots, N$. In other words, $u_l \leq \text{BED}^m_{\max}/(N \min_{i \in \mathcal{I}_l} A_{i,l})$. Thus, the feasible region is bounded. It is also closed, as all constraint functions are continuous. Moreover, the objective function in [P($\vec{w};N$)] is also continuous. Thus, [P($\vec{w};N$)] has an optimal solution as claimed. □

Endnote

[1] Based on our analysis in Saberian et al. (2016), $1 + T_{\text{lag}}$ is likely to be a lower bound on the optimal number of fractions; thus, when N^*_{99} was smaller than $1 + T_{\text{lag}}$, it was reset to $1 + T_{\text{lag}}$.

References

Ahamad A, Rosenthal DI, Ang KK (2005) Altered fractionation. Adelstein DJ, ed. *Squamous Cell Head and Neck Cancer: Recent Clinical Progress and Prospects for the Future*, Current Clinical Oncology (Humana Press, Totowa, NJ), 125–144.

Arcangeli G, Saracino B, Gomellini S, Petrongari MG, Arcangeli S, Sentinelli S, Marzi S, Landoni V, Fowler J, Strigari L (2010) A prospective phase III randomized trial of hypofractionation versus conventional fractionation in patients with high-risk prostate cancer. *Internat. J. Radiation Oncology Biol. Phys.* 78(1):11–18.

Armpilia CI, Dale RG, Jones B (2004) Determination of the optimum dose per fraction in fractionated radiotherapy when there is delayed onset of tumour repopulation during treatment. *British J. Radiology* 77(921):765–767.

Bortfeld T, Ramakrishnan J, Tsitsiklis JN, Unkelbach J (2015) Optimization of radiation therapy fractionation schedules in the presence of tumor repopulation. *INFORMS J. Comput.* 27(4): 788–803.

Breedveld S, Storchi PRM, Keijzer M, Heijmen BJM (2006) Fast, multiple optimizations of quadratic dose objective functions in IMRT. *Phys. Medicine Biol.* 51(14):3569–3579.

Brenner DJ (2004) Fractionation and late rectal toxicity. *Internat. J. Radiation Oncology Biol. Phys.* 60(4):1013–1015.

Brenner DJ, Hall EJ (1999) Fractionation and protraction for radiotherapy of prostate carcinoma. *Internat. J. Radiation Oncology Biol. Phys.* 43(5):1095–1101.

Burman C, Chui C-S, Kutcher G, Leibel S, Zelefsky M, LoSasso T, Spirou S, et al. (1997) Planning, delivery, and quality assurance of intensity-modulated radiotherapy using dynamic multileaf collimator: A strategy for large-scale implementation for the treatment of carcinoma of the prostate. *Internat. J. Radiation Oncology Biol. Phys.* 39(4):863–873.

Choi B, Deasy JO (2002) The generalized equivalent uniform dose function as a basis for intensity-modulated treatment planning. *Phys. Medicine Biol.* 47(20):3579–3589.

Ehrgott M, Guler C, Hamacher HW, Shao L (2008) Mathematical optimization in intensity modulated radiation therapy. *4OR* 6(3):199–262.

Eisbruch A (2002) Intensity-modulated radiotherapy of head-and-neck cancer: Encouraging early results. *Internat. J. Radiation Oncology Biol. Phys.* 53(1):1–3.

Emami B, Lyman J, Brown A, Coia L, Goiten M, Munzenride JE, et al. (1991) Tolerance of normal tissue to therapeutic radiation. *Internat. J. Radiation Oncology Biol. Phys.* 21(1):109–122.

Fiacco AV, Kyparisis J (1986) Convexity and concavity properties of the optimal value function in parametric nonlinear programming. *J. Optim. Theory Appl.* 48(1):95–126.

Fowler JF (1984) Non-standard fractionation in radiotherapy. *Internat. J. Radiation Oncology Biol. Phys.* 10(5):755–759.

Fowler JF (1990) How worthwhile are short schedules in radiotherapy?: A series of exploratory calculations. *Radiotherapy Oncology* 18(2):165–181.

Fowler JF (2001) Biological factors influencing optimum fractionation in radiation therapy. *Acta Oncologica* 40(6):712–717.

Fowler JF (2007) Is there an optimal overall time for head and neck radiotherapy? A review with new modeling. *Clinical Oncology* 19(1):8–27.

Fowler JF (2008) Optimum overall times. II: Extended modelling for head and neck radiotherapy. *Clinical Oncology* 20(2):113–126.

Fowler JF, Ritter MA (1995) A rationale for fractionation for slowly proliferating tumors such as prostatic adenocarcinoma. *Internat. J. Radiation Oncology Biol. Phys.* 32(2):521–529.

Fowler JF, Chappell R, Ritter M (2001) Is alpha/beta for prostate tumors really low? *Internat. J. Radiation Oncology Biol. Phys.* 50(4):1021–1031.

Fu KK, Pajak TF, Trotti A, Jones CU, Spencer SA, Phillips TL, Garden AS, Ridge JA, Cooper JS, Ang KK (2000) A radiation therapy oncology group (RTOG) phase III randomized study to compare hyperfractionation and two variants of accelerated fractionation to standard fractionation radiotherapy for head and neck squamous cell carcinomas: First report of RTOG 9003. *Internat. J. Radiation Oncology Biol. Phys.* 48(1):7–16.

Gao M, Mayr NA, Huang Z, Zhang H, Wang JZ (2010) When tumor repopulation starts: The onset time of prostate cancer during radiation therapy. *Acta Oncologica* 49(8):1269–1275.

Garden AS (2001) Altered fractionation for head and neck cancer. *Oncology* 15(10):1326–1332.

Grant M, Boyd S (2009) CVX: MATLAB software for disciplined convex programming (web page and software). Accessed February 27, 2017, http://cvxr.com/cvx.

Gu X, Choi D, Men C, Pan H, Majumdar A, Jiang SB (2009) GPU-based ultrafast dose calculation using a finite size pencil beam model. *Phys. Medicine Biol.* 54(20):6287–6297.

Hall EJ, Giaccia AJ (2005) *Radiobiology for the Radiologist* (Lippincott Williams & Wilkins, Philadelphia).

Haustermans KMG, Hofland I, Poppel HV, Oyen R, Van de Voorde W, Begg AC, Fowler JF (1997) Cell kinetic measurements in prostate cancer. *Internat. J. Radiation Oncology Biol. Phys.* 37(5): 1067–1070.

Ho KF, Fowler JF, Sykes AJ, Yap BK, Lee LW, Slevin NJ (2009) IMRT dose fractionation for head and neck cancer: Variation in current approaches will make standardisation difficult. *Acta Oncologica* 48(3):431–439.

Horiot JC, Le Fur R, N'Guyen T, Chenal C, Schraub S, Alfonsi S, Gardani G, Van Den Bogaert W, Danczak S, Bolla M (1992) Hyperfractionation versus conventional fractionation in oropharyngeal carcinoma: Final analysis of a randomized trial of the EORTC cooperative group of radiotherapy. *Radiotherapy Oncology* 25(4):231–241.

Horiot JC, Bontemps P, Van Den Bogaert W, Fur RL, Van Den Weijngaert D, Bolla M, Bernier J, et al. (1997) Accelerated fractionation (AF) compared to conventional fractionation (CF) improves loco-regional control in the radiotherapy of advanced head and neck cancers: Results of the EORTC 22851 randomized trial. *Radiotherapy and Oncology: J. Eur. Soc. Therapeutic Radiology Oncology* 44(2):111–121.

Jeraj R, Keall P (1999) Monte carlo-based inverse treatment planning. *Phys. Medicine Biol.* 44(8):1885–1896.

Joiner M, van der Kogel A (2009) *Basic Clinical Radiobiology*, 4th ed. (Hodder Arnold, London).

Jones B, Tan LT, Dale RG (1995) Derivation of the optimum dose per fraction from the linear quadratic model. *British J. Radiology* 68(812):894–902.

Kader HA, Mydin AR, Wilson M, Alexander C, Shahi J, Pathak I, Wu JS, Truong PT (2011) Treatment outcomes of locally advanced oropharyngeal cancer: A comparison between combined modality radio-chemotherapy and two variants of single modality altered fractionation radiotherapy. *Internat. J. Radiation Oncology Biol. Phys.* 80(4):1030–1036.

Kehwar TS (2005) Analytical approach to estimate normal tissue complication probability using best fit of normal tissue tolerance doses into the ntcp equation of the linear quadratic model. *J. Cancer Res. Therapy* 1(3):168–179.

Keller H, Meier G, Hope A, Davison M (2012) SU-E-T-461: Fractionation schedule optimization for lung cancer treatments using radiobiological and dose distribution characteristics. *Medical Phys.* 39(6):3811.

Kim M, Ghate A, Phillips MH (2012) A stochastic control formalism for dynamic biologically conformal radiation therapy. *Eur. J. Oper. Res.* 219(3):541–556

Kyparisis J, Fiacco AV (1987) Generalized convexity and concavity of the optimal value function in nonlinear programming. *Math. Programming* 39(3):285–304.

Langer M, Lee EK, Deasy JO, Rardin RL, Deye JA (2003) Operations research applied to radiotherapy. An NCI-NSF-sponsored workshop—February 7–9, 2002. *Internat. J. Radiation Oncology Biol. Phys.* 57(3):762–768.

Luo Z-Q, Ma W-K, So AMC, Ye Y (2010) Semidefinite relaxation of quadratic optimization problems. *IEEE Signal Processing Magazine* 27(3):20–34.

Marks LB, Yorke ED, Jackson A, Haken RKT, Constine LS, Eisbruch A, Bentzen SM, Nam J, Deasy JO (2010) Use of normal tissue complication probability models in the clinic. *Internat. J. Radiation Oncology Biol. Phys.* 76(3):S10–S19.

Marzi S, Saracino B, Petrongari M, Arcangeli S, Gomellini S, Arcangeli G, Benassi M, Landoni V (2009) Modeling of alpha/beta for late rectal toxicity from a randomized phase II study: Conventional versus hypofractionated scheme for localized prostate cancer. *J. Experiment. Clinical Cancer Res.* 28(1): 117–124.

Mavroidis P, Ferreira BC, do Carmo Lopes M (2011) Response-probability volume histograms and iso-probability of response charts in treatment plan evaluation. *Medical Phys.* 38(5): 2382–2397.

Mayles P, Nahum A, Rosenwald JC, eds. (2007) *Handbook of Radiotherapy Physics: Theory and Practice* (Taylor and Francis, Boca Raton, FL).

Men C, Gu X, Choi D, Majumdar A, Zheng Z, Mueller K, Jiang SB (2009) GPU-based ultrafast IMRT plan optimization. *Phys. Medicine Biol.* 54(21):6565–6573.

Mizuta M, Takao S, Date H, Kishimoto N, Sutherland KL, Onimaru R, Shirato H (2012) A mathematical study to select fractionation regimen based on physical dose distribution and the linear-quadratic model. *Internat. J. Radiation Oncology Biol. Phys.* 84(3):829–833.

Niemierko A (1997) Reporting and analyzing dose distributions: A concept of equivalent uniform dose. *Medical Phys.* 24(1):103–110.

Qi XS, Yang Q, Lee SP, Li XA, Wang D (2012) An estimation of radiobiological parameters for head-and-neck cancer cells and the clinical implications. *Cancers* 4(2):566–580.

Rockwell S (1998) Experimental radiotherapy: A brief history. *Radiation Res.* 150(Supplement):S157–S169.

Romeijn HE, Dempsey JF (2008) Intensity modulated radiation therapy treatment plan optimization. *TOP* 16(2):215–243.

Romeijn HE, Ahuja RK, Dempsey JF, Kumar A (2006) A new linear programming approach to radiation therapy treatment planning problems. *Oper. Res.* 54(2):201–216.

Saberian F, Kim M (2014) Phantom Creator (PhanC): A MATLAB software for creating phantom test cases for IMRT optimization, working draft of the user's manual. University of Washington, Seattle.

Saberian F, Ghate A, Kim M (2015) A two-variable linear program solves the standard linear-quadratic formulation of the fractionation problem in cancer radiotherapy. *Oper. Res. Lett.* 43(3): 254–258.

Saberian F, Ghate A, Kim M (2016) Optimal fractionation in radiotherapy with multiple normal tissues. *Math. Medicine Biol.* 33(2): 211–252.

Salari E, Romeijn HE (2012) Quantifying the trade-off between IMRT treatment plan quality and delivery efficiency using direct aperture optimization. *INFORMS J. Comput.* 24(4):518–533.

Shepard DM, Ferris MC, Olivera GH, Mackie TR (1999) Optimizing the delivery of radiation therapy to cancer patients. *SIAM Rev.* 41(4):721–744.

Siebers JV, Tong SD, Lauterbach M, Wu QW, Mohan R (2001) Acceleration of dose calculations for intensity-modulated radiotherapy. *Medical Phys.* 28(6):903–910.

Spirou SV, Chui CS (1998) A gradient inverse planning algorithm with dose-volume constraints. *Medical Phys.* 25(3):321–333.

Thames HD, Bentzen SM, Turesson I, Overgaard M, van den Bogaert W (1989) Fractionation parameters for human tissues and tumors. *Internat. J. Radiation Biol.* 56(5):701–710.

Tian Z, Zarepisheh M, Jia X, Jiang SB (2013) The fixed-point iteration method for IMRT optimization with truncated dose deposition coefficient matrix. Technical report, Center for Advanced Radiotherapy Technologies and Department of Radiation Medicine and Applied Sciences, University of California San Diego, La Jolla, CA. https://arxiv.org/ftp/arxiv/papers/1303/1303.3504.pdf.

Trotti A, Fu KK, Pajak TF, Jones CU, Spencer SA, Phillips TL, Garden AS, Ridge JA, Cooper JS, Ang KK (2005) Long term outcomes of RTOG 90–03: A comparison of hyperfractionation and two variants of accelerated fractionation to standard fractionation radiotherapy for head and neck squamous cell carcinoma. *Internat. J. Radiation Oncology Biol. Phys.* 63(Supplement 1):S70–S71.

Unkelbach J, Zeng C, Engelsman M (2013a) Simultaneous optimization of dose distributions and fractionation schemes in particle radiotherapy. *Medical Phys.* 40(9):091702.

Unkelbach J, Craft D, Saleri E, Ramakrishnan J, Bortfeld T (2013b) The dependence of optimal fractionation schemes on the spatial dose distribution. *Phys. Medicine Biol.* 58(1):159–167.

Wang JZ, Guerrero M, Li XA (2003) How low is the alpha/beta ratio for prostate cancer? *Internat. J. Radiation Oncology Biol. Phys.* 55(1):194–203.

Webb S (2010) *Contemporary IMRT: Developing Physics and Clinical Implementation* (IOP Publishing, Bristol, UK).

Webb S, Oldham M (1996) A method to study the characteristics of 3D dose distributions created by superposition of many intensity-modulated beams delivered via a slit aperture with multiple absorbing vanes. *Phys. Medicine Biol.* 41(10): 2135–2153.

Webb S, Convery DJ, Evans PM (1998) Inverse planning with constraints to generate smoothed intensity-modulated beams. *Phys. Medicine Biol.* 43(10):2785–2794.

Williams MV, Denekamp J, Fowler JF (1985) A review of alpha/beta ratios for experimental tumors: Implications for clinical studies of altered fractionation. *Internat. J. Radiation Oncology Biol. Phys.* 11(1):87–96.

Yang Y, Xing L (2005) Optimization of radiotherapy dose-time fractionation with consideration of tumor specific biology. *Medical Phys.* 32(12):3666–3677.